Molecular Interactions of Plutonium(VI) with Synthetic Manganese-Substituted Goethite

Yung-Jin Hu[1, 2], Luna Kestrel Schwaiger[1, 2], Corwin H. Booth[3], Ravi K. Kukkadapu[4], Elena Cristiano[2], Daniel Kaplan[5], and Heino Nitsche[1, 2, *]

[1]Department of Chemistry, University of California, Berkeley, CA 94720

[2]Nuclear Sciences Division, Lawrence Berkeley National Laboratory, Berkeley, CA 94720

[3]Chemical Sciences Division, Lawrence Berkeley National Laboratory, Berkeley, CA 94720

[4]Pacific Northwest National Laboratory, Richland, WA 99352

[5]Savannah River National Laboratory, Aiken, SC 29808

*Corresponding author: HNitsche@lbl.gov, 510.486.5615

Keywords

plutonium, XAS, redox, sorption, manganese-substituted goethite, iron

Summary

Plutonium(VI) sorption on the surface of well-characterized synthetic manganese-substituted goethite minerals ($Fe_{1-x}Mn_xOOH$) was studied using X-ray absorption spectroscopy. We chose to study the influence of manganese as a minor component in goethite, because goethite rarely exists as a pure phase in nature. Manganese X-ray absorption near-edge structure measurements indicated that essentially all the Mn in the goethite existed as Mn(III), even though Mn was added during mineral synthesis as Mn(II). Importantly, energy dispersive X-ray analysis demonstrated that Mn did not exist as discrete phases and that it was homogeneously mixed into the goethite to within the limit of detection of the method. Furthermore, Mössbauer spectra demonstrated that all Fe existed as Fe(III), with no Fe(II) present. Plutonium(VI) sorption experiments were conducted open to air and no attempt was made to exclude carbonate. The use of X-ray absorption spectroscopy allows us to directly and unambiguously measure the oxidation state of plutonium in situ at the mineral surface. Plutonium X-ray absorption near-edge structure measurements carried out on these samples showed that Pu(VI) was reduced to Pu(IV) upon contact with the mineral. This reduction appears to be strongly correlated with mineral solution pH, coinciding with pH transitions across the point of zero charge of the mineral. Furthermore, extended X-ray absorption fine structure

measurements show evidence of direct plutonium binding to the metal surface as an inner-sphere complex. This combination of extensive mineral characterization and advanced spectroscopy suggests that sorption of the plutonium onto the surface of the mineral was followed by reduction of the plutonium at the surface of the mineral to form an inner-sphere complex. Because manganese is often found in the environment as a minor component associated with major mineral components, such as goethite, understanding the molecular-level interactions of plutonium with such substituted-mineral phases is important for risk assessment purposes at radioactively contaminated sites and long-term underground radioactive waste repositories.

1 Introduction

Plutonium can exist simultaneously in the environment as Pu(III), Pu(IV), Pu(V), and Pu(VI) [1], but mainly exists as the three higher oxidation states [Pu(IV), Pu(V), and Pu(VI)] in oxic waters [2]. Pu(V) and Pu(VI) exist in solution as the plutonyl moiety (PuO_2^{n+}) with effective aqueous solution charge, n, of +2.3 and +3.3, respectively [3]. This reduced effective charge, as compared to Pu(IV), results in the oxidized forms of plutonium being more soluble and, by extension, more mobile in the environment. This result has been experimentally measured in the past, showing that Pu(IV) is many orders of magnitude more insoluble than the oxidized Pu(V) and Pu(VI) forms [1]. Previous work by Kaplan et al. [4] using laboratory and lysimeter studies showed that > 95% of plutonium migrating from a purposefully placed solid $Pu^{IV}(NO_3)_4$ source remained within 1.25 cm of the source over an 11 year period under natural environmental conditions at the Department of Energy (DOE) Savannah River Site (SRS). Such work on large-scale environmental systems is an important part in uncovering essential components of the soil and mineral composition that controls plutonium redox chemistry. However, individual sorption and redox processes must also be tested on well-characterized model mineral phases that properly represent individual environmental components. Shaughnessy et al. [5] have shown the capacity of the pure manganese minerals manganite (γ-$Mn^{III}OOH$) and hausmannite ($Mn^{II}Mn^{III}_2O_4$) to reduce plutonium from the hexavalent to the tetravalent form using X-ray absorption spectroscopy (XAS). Similar sorption studies of Pu(V) on magnetite ($Fe^{II}Fe^{III}_2O_4$) [6, 7] using solvent extraction also showed reduction to Pu(IV). However, previous XAS measurements involving goethite, $Fe^{III}O(OH)$ [8], a mineral devoid of Fe(II), showed reduction of Pu(VI) to Pu(V) at micromolar to millimolar concentrations, but no evidence of further reduction to Pu(IV). Powell et al. [9] and Keeney-Kennicutt and Morse

[10] observed Pu(V) reduction by goethite to Pu(IV); neither identified the source of the reductant. Duff et al. [11, 12] observed oxidation of Pu(V) to Pu(VI) on the surface of Yucca Mountain Tuff in the vicinity of manganese-containing minerals using the μ-XAS technique. Measurements on the same sample 2 years later, by Powell et al. [7], however, show that the majority of the plutonium eventually reduced to Pu(IV).

In nature, manganese is rarely found as a pure mineral phase. It is often found as a minor component associated with major mineral phases, such as goethite. As a model to these environmental minerals, we have synthesized and extensively characterized manganese-substituted goethite with a small mole-fraction of manganese substituted into the goethite crystal structure. The purpose of this study was to acquire a molecular-level understanding of the sorption processes and redox reactions that are occurring between Pu(VI) and the surface of these synthesized manganese-substituted goethite minerals. Understanding such fundamental properties are essential in the proper modeling and risk-analysis of plutonium storage in underground geological repositories.

2 Materials and Methods

2.1 Mn-Substituted Goethite Synthesis

Manganese substituted (Mn-substituted) goethite (Table 1) was synthesized by adapting a procedure from Schwertmann and Cornell [13-15]. Reagent grade $FeCl_3 \cdot 6H_2O$ and $MnCl_2 \cdot 4H_2O$ were used instead of $Fe(NO_3)_3 \cdot 9H_2O$ and $Mn(NO_3)_2 \cdot 4H_2O$, and NaOH was used instead of KOH. The precipitate was washed repeatedly with 18.2 MΩ (Milli-Q) water and then suspended in dialysis tubing (SnakeSkin Pleated Dialysis Tubing 3500 MWCO) in Milli-Q water exchange solution until the conductivity of the exchange solution was < 2.0 μS. The sieved 63-212 μm fraction of the Mn-substituted goethite was used in the following experiments.

2.2 Mn-Substituted Goethite Characterization

Manganese percent substitution into the goethite substructure was measured by inductively coupled plasma – mass spectrometry (ICP-MS). Synthesized goethite samples were fully dissolved in a solution of 1 M oxalic acid and 0.01 M L-ascorbic acid at room temperature. These solutions were then filtered, properly diluted, and the elemental composition of Mn and Fe measured using a Perkin-Elmer Elan DRC II ICP-MS with a Sc or Ga internal standard.

The Mn-substituted goethite surface area was determined using a 5-point BET N_2 adsorption on an ASAP 2010 Micromeritics Instrument (Norcross, GA). A NIST standard was included with these samples: NIST SRN 1900 Si $_3N_4$ with a surface area of 2.84 ± 0.09 m^2/g. This standard was measured to be 2.83 m^2/g, which is within the error bar of the NIST standard.

Point of zero charge (PZC) measurements were conducted on the Mn-substituted goethite using the powder addition method [16, 17]. This method was chosen because of two distinct advantages: the process is fast, and it requires a small amount of mineral compared to other methods, such as potentiometric titration [18] and mass titration [19]. A set of 0.01 M $NaClO_4$ solutions were adjusted to pH 3 – 10 in whole pH units using carbonate-free NaOH and $HClO_4$. The initial pH (pH_i) was recorded and a given amount of solid (5 g/L) was added to each solution. The tubes, back-filled with argon, were placed on a rocker-shaker and allowed to equilibrate. The final (pH_f) was measured after 24 h at 25 ± 1 ºC. The ΔpH (pH_f - pH_i) was plotted versus pH_i and the value on the curve where ΔpH was equal to zero was taken to be the PZC. The final pH values were regularly checked for 50 days and the PZC values were constant during the whole period.

Powder X-ray diffraction (XRD) spectra of pure goethite (Alfa Aesar) and Mn-substituted goethite were recorded using a Panalytical X'Pert Pro powder X-ray diffractometer using Cu-K_α radiation and a Ni filter on dried and finely ground mineral samples. The mineral powder (received with Na^+ on the exchange sites) was placed on a zero background plate with a thin layer of immersion oil. Data was collected over a two theta angle (2θ) from 10.0º to 70.0º. Data processing involved fitting and subtracting a smooth polynomial background from each scan to facilitate comparisons between scans. Scanning electron microscopy was conducted on the Mn-substituted goethite using a LEO Model 440 (Peabody, MA) and the energy dispersive X-ray analysis was conducted on an INCAWave 7060 (Oxford Instruments, Concord MA).

Mössbauer spectra were collected for the Mn-substituted goethite using a 50 mCi (initial strength) ^{57}Co/Rh source. The velocity transducer MVT-1000 (WissEL) was operated in a constant acceleration mode (23 Hz, ±12 mm/s). An Ar-Kr proportional counter was used to detect the radiation transmitted through the holder, and the counts were

stored in a multichannel scalar (MCS) as a function of energy (transducer velocity) using a 1024-channel analyzer. Data were folded to 512 channels to give a flat background and a zero-velocity position corresponding to the center shift (CS) of a metal Fe foil at room temperature. Calibration spectra were obtained with a 25 μm thick Fe metal foil (Amersham, England) placed in the same position as the samples to minimize any errors due to changes in geometry. The Mössbauer data were modeled with Recoil software (University of Ottawa, Canada) using a Voigt-based structural fitting routine [20]. The coefficient of variation of the spectral areas of the individual sites generally ranged between 1% and 2% of the fitted values. A closed cycle cryostat (Janis) was used for measurements below room temperature.

2.3 Speciation Diagram Calculation

Plutonium solution speciation diagrams were calculated using the in-house code SPECIATE, which statistically samples thermodynamic databases with associated error [21] using the Monte Carlo sampling method. Pseudo-random number generation is handled by the Mersenne Twister algorithm [22]. SPECIATE utilizes the PHREEQC code [23] to calculate the actual speciation in solution for a particular set of randomly sampled thermodynamic values. The output is then analyzed and asymmetric error bands are determined for the species in solution at the 1σ level.

2.4 Pu(VI) Preparation

Solutions of $^{239}Pu(VI)$ in the form PuO_2^{2+} were prepared by fuming a plutonium stock solution with concentrated nitric acid to destroy any organic material that might have been present as a safety precaution. This process was repeated three times. The solution was then refluxed twice with concentrated perchloric acid (70% double distilled from VYCOR, G.F.Smith) to oxidize the solution to Pu(VI). **Caution: The presence of any organic material, even the smallest amounts, may cause an explosion when placed in contact with hot perchloric acid!** Manipulation of plutonium was performed in a negative pressure glovebox. All steps involving concentrated nitric and perchloric acids were performed in specially designed glassware to prevent the accumulation of hot acid vapors inside the glovebox and to prevent the formation of explosive perchlorate compounds. The stock solution was then diluted to about 1 M $HClO_4$. Plutonium oxidation state in the stock solution was confirmed by UV-Vis spectroscopy using an OceanOptics S2000 fiber-optic spectrometer. Spectra showed only the presence of Pu(VI) in solution [24].

2.5 XAS Sample Preparation

Approximately 100 mg of each mineral was placed in separate vials with approximately 8 mL of pH 5.5 solution held at a constant ionic strength of 0.1 M with $NaClO_4$ and open to air. Sufficient PuO_2^{2+} was loaded into each vial to bring the total Pu solution concentration to 250 μM and the pH was quickly adjusted using small amounts of $HClO_4$ and NaOH. The relatively high concentrations of plutonium are required to acquire high-quality XAS data [25]. Samples were placed on a rocker and allowed to equilibrate for 48 hours. Following equilibration, samples were loaded as wet pastes into Kapton tubes and triply contained before transporting to the synchrotron for measurement. A separate aliquot of the solution in contact with the mineral was taken, filtered through a Microcon Ultracel YM-30 centrifugal filter (regenerated cellulose 30,000 MWCO) and counted using a Wallac 1414 liquid scintillation counter running in α/β discrimination mode to measure the percent plutonium sorbed on the mineral.

2.6 XAS Measurements

All sample spectra were collected at 50 K, using a specially-engineered liquid helium cryostat (Janis), to mitigate beam-induced reduction of the sample. The effect of beam-induced reduction of Pu(VI) and Pu(V) to Pu(IV) on pure goethite at room temperature has been observed in the past and is hypothesized to be caused by radiolytic reactions within the system [8]. The vertical aperture of the beam in all cases was held at 0.5 mm.

Manganese K-edge X-ray absorption near-edge structure (XANES) spectra were collected at the Stanford Synchrotron Radiation Lightsource (SSRL) on beamline 10-2 using a fully tuned Si(220) φ-90° double-crystal monochromator with a harmonic rejection mirror set to an 8 keV cut-off. Data were collected in fluorescence mode using a 13-element germanium detector. Count rates were sufficiently low that a dead time correction was unnecessary. Energy calibration was performed in transmission mode by simultaneously measuring the manganese K-edge of a manganese metal foil.

Plutonium L_{III}-edge XANES spectra were collected at SSRL on beamline 11-2 using a 30% detuned Si(220) φ-0° double-crystal monochromator. Data were collected in fluorescence mode using a 32-element germanium detector.

A dead time correction was applied to the spectra. Energy calibration was performed in transmission mode by measuring the plutonium L_{III}-edge of a $^{242}PuO_2$ powder reference between scans.

Raw data were pre-edge subtracted and normalized using the Real-Space X-ray Analysis Package (RSXAP) [26, 27], a software package for XAS data analysis. Manganese XANES spectra were energy calibrated by setting the first inflection point of the K-edge of a manganese metal reference sample to be 6540.0 eV [28]. Plutonium XANES spectra were energy calibrated by setting the first inflection point of the L_{III}-edge of a PuO_2 reference sample to be 18062.3 eV [29]. Plutonium oxidation state percentages were acquired through least-squares fitting of normalized Pu(IV), Pu(V), and Pu(VI) standard XANES spectra [30]. Plutonium extended X-ray absorption fine structure (EXAFS) spectra were isolated using standard procedures [27] and fit to ab-initio calculated scattering paths from the FEFF7 [31] code out to a k-range of 12 $Å^{-1}$. The number of varied parameters in the fits was limited to be less than the number of independent data points in the spectrum (N_i). N_i is calculated using the adjusted Nyquist limit equation, $N_i = 2\Delta k \Delta R/\pi + 2$, where Δk is the k-range over which the fit is conducted and ΔR is the r-range over which the fit is being conducted [32]. S_o^2 for the fits was constrained to 1. Asymmetric error bars were calculated for the fits using the method outlined by Booth et al. [33].

3 Results and Discussion

3.1 Mineral Synthesis and Characterization

Slight changes were made to the synthesis procedure from Schwertmann and Cornell [13-15] to ensure that nitrates were not present in the final mineral because nitrate complexation with plutonium may influence its redox chemistry. The laboratory synthesis of Mn-substituted goethite requires relatively large amounts of strong base. The removal of this base after synthesis is therefore necessary to ensure a clean material for proper characterization and plutonium sorption experiments.

The 63-212 μm size fraction of the two Mn-substituted minerals that were synthesized for this study, MG-1.0 and MG-0.5, were analyzed using ICP-MS to quantify the exact manganese substitution (Table 1). Measured values were in agreement with initial target synthesis values. BET measurements were conducted to measure surface area and were shown to be less than that of pure goethite. The PZC of the minerals were measured for comparison to

194 pure goethite and as a guide in planning plutonium sorption measurements. These data are presented in Table 1 and
195 indicates that the greater the Mn substitution, the lower the PZC. The implication of this is that at paraneutral pH
196 levels, we would expect greater plutonium electrostatic attraction to the 1% than the 0% or 0.5% substituted goethite
197 samples.
198
199 Powder XRD of the synthesized mineral (Figure 1) showed Bragg peaks indicative of the goethite structure with no
200 significant shifts. Such shifts in the Bragg reflections are present in Mn-substituted goethite with larger manganese
201 percent substitutions and have previously been shown to be caused by the shrinking of the a-, and c-crystallographic
202 parameters and the expansion of the b-parameter resulting from increased manganese substitution into the goethite
203 crystal lattice [34].
204
205 SEM measurements (Figure 2) indicates that the mineral is crystalline and that sieving is isolating the proper mineral
206 size fraction. Close inspection of the micrographs (in the 1μm range) shows the following morphologies: round rod-
207 like structures for pure goethite and an increase in the length-to-width ratio in crystal growth for Mn-substituted
208 goethite as compared to pure goethite. This result is in agreement with previous studies [34-36]. Importantly, EDX
209 measurements on the synthesized minerals showed the presence of manganese, homogeneity in the substitution for
210 iron at the mineral surface to within the resolution of the method, and that the manganese did not exist as discrete
211 phases within the goethite minerals.
212
213 ^{57}Fe-specific Mössbauer spectroscopy was employed to characterize the Mn-substituted goethite for purity and
214 confirm manganese incorporation. Mössbauer spectra of both MG-0.5 and MG-1.0 were collected at room
215 temperature and 77 K. At both the temperatures, the spectral sextet features of the samples are similar to each other;
216 the similarity is apparent from a comparison of their room temperature spectra (Figure 3a). The similarity of the
217 samples is also evident from the modeled hyperfine field distribution (Figure 3b). The derived hyperfine field
218 parameters of the samples are slightly lower than that of pure goethite, implying substitution of Mn. Absence of
219 doublet peaks in both room temperature and 77 K (not shown) spectra is in agreement with the absence of relatively
220 small goethite particles (< 8 nm), and the absence of poorly-crystalline Fe-oxides. Furthermore, the spectra show
221 that the iron in the synthesized mineral is in the form Fe(III), with no Fe(II) present.

XANES measurements for the Mn-substituted minerals (Figure 4) show that the position of the characteristic white line coincides with that of the Mn(III) reference compound $LaMn^{III}O_3$, suggesting that manganese is substituted into the goethite structure in the trivalent state. Schwertmann and Cornell [13] propose that, although added as Mn(II), the manganese is oxidized and incorporated into the mineral as Mn(III) during the synthesis. Our direct spectroscopic measurement is in agreement with previous work by Alvarez et al. [35]. It is important to note, however, the slight shoulder on the Mn-substituted goethite XANES spectra at approximately 6550 eV. This shoulder is also present in the spectra taken by Alvarez et al. [35] and does not rule out the possibility of small amounts of Mn(II) present in the mineral. The shoulder could also be caused by the presence of pre-edge features arising from a dipole-forbidden transition to an unoccupied energy state.

3.2 Plutonium(VI) Speciation Calculation

A plutonium(VI) solution speciation diagram was calculated from the thermodynamic data in Table 2, and is shown in Figure 5. Knowledge of the presence or absence of plutonium species in solution as a function of pH is an important factor in understanding the kinds of plutonium complexes available for sorption onto the mineral surface. For elements that have precisely measured thermodynamic formation constants it is sufficient to simply use the average measured values to calculate a speciation diagram since propagated errors in the speciation diagram will be small. However, in the case of many plutonium species, where measured formation constants have large associated measurement errors, it is essential to take into account these measured errors when calculating speciation diagrams. Examination of Table 2 shows that associated errors are as high as ± 1.5 for some plutonium complexes. Note that the values listed are the base-10 logarithm of the formation constant so an error of ± 1.0 represents an error in the measurement of the formation constant by one order of magnitude on either side. Such large errors in the formation constant manifest themselves in the large error bands in the calculated speciation diagram shown in Figure 5. Previous work has been done on the subject of propagating errors into speciation diagrams using both Monte Carlo and Latin hypercube sampling methods, resulting in LJUNGSKILE [37, 38], a freely available program for the Windows operating system. Although SPECIATE borrows heavily from LJUNGSKILE's basic internal design, it has been written from scratch to take advantage of parallel computer processing and allows for more direct

interaction with the underlying PHREEQC program. We use the results from the speciation diagram calculation below to assist us in the modeling of mineral surface structures in the EXAFS fits.

3.3 Plutonium XANES Spectral Fits

Plutonium XANES measurements provide a direct, in situ, method for measuring the valence state of the plutonium atom present in the mineral solution in a non-destructive way. Figure 6 shows a representative fit of the Pu L_{III}-edge to pure oxidation state standards. The slight shoulder to the high energy side of the white line is a result of multiple-scattering effects of the photoelectron off of the two axial oxygens present in the higher plutonium oxidation states. This feature can be seen in the scaled Pu(V) component but is absent in the scaled Pu(IV) component. Results from the plutonium XANES measurements are shown in Table 3. The percent of plutonium sorbed onto the mineral surface is lower than in previous experiments involving sorption of Pu(VI) to pure goethite [8]. However, this is expected because we are working at higher plutonium concentrations. The results from XANES measurements show reduction of plutonium from the more soluble Pu(VI) to the more insoluble Pu(IV) upon introduction to the mineral solution. Particularly important is the pH dependence for reduction. Table 3 shows that despite the small increase in Pu sorption upon increasing the solution pH from 6.05 to 7.63 for the MG-0.5 mineral, we see a significant (40 ± 7%) increase in the ability of the mineral to reduce Pu(VI) to Pu(IV). This increase in pH coincides with the transition of the mineral solution pH across the PZC of the mineral (PZC = 6.78 ± 0.05; Table 1). The point of zero charge, as measured by the powder addition method, is more appropriately called the point of net zero proton charge. This value represents the pH at which the surface of the mineral in the mineral solution has a net zero charge. At pH values below the point of zero charge the mineral surface carries a net positive charge, while at pH values above the point of zero charge the mineral surface carries a net negative charge. Positively charged or neutral species are therefore at an electrostatic disadvantage for sorption onto the surface of the mineral at lower pH values (Figure 5). As the mineral solution pH increases above the PZC, the electrostatic interaction between the mineral surface and metal ions favors electrostatic sorption onto the surface as either an inner-sphere complex (directly bound to the mineral surface) or as an outer-sphere complex. The significant increase in plutonium reduction upon increasing the solution pH suggests that the plutonium is being reduced to Pu(IV) through a surface-mediated mechanism. Such mechanisms have been proposed in the past for Pu(VI) on hausmanite ($Mn^{II}Mn^{III}{}_2O_4$) and manganite (γ-$Mn^{III}OOH$) [5] through the use of XAS measurements, and for Pu(V) on magnetite ($Fe^{II}Fe^{III}{}_2O_4$) [6, 7] using solvent extraction

methods. Furthermore, this data suggest that it is unlikely that surface accumulation of Pu(V) followed by disproportionation to Pu(IV) and Pu(VI) is the major mechanism of reduction occurring at the solution-mineral surface. If such a mechanism controlled the redox chemistry at the solution-mineral surface the plutonium reduction would be expected to change as a function of the total amount of plutonium sorbed onto the mineral surface.

3.4 Plutonium EXAFS Spectral Fits

Figure 7 shows EXAFS spectra fits in both k-space and r-space with the accompanying fit parameters given in Table 4. In the following discussion of the EXAFS spectra, Fourier transform (FT) peak positions are reported in units of Å with no correction for phase shift (r+Δ). In contrast, when referring to bond lengths, we report actual distances in units of Å.

MG-0.5 pH 6.05 distinctly shows the well known "split-oxygen" shell associated with the actinyl moiety [39]. This spectral feature arises from interference between the EXAFS oscillations of the axial and equatorial oxygens. EXAFS fits for this split-oxygen shell show an expansion of the axial Pu-O bond length to approximately 1.85 Å, suggesting that the plutonium is in the pentavalent form as our XANES fits above indicate. Models for the other two samples also take into account the smaller percentage of Pu(V) present by fitting a Pu-O_{ax} single-scattering (SS) path and a Pu-O_{ax1}-Pu-O_{ax2} multiple-scattering (MS) path with coordination numbers, N_{SS} and N_{MS}, constrained to the percent Pu(V) determined in the XANES fits. Other parameters for the MS were highly constrained to the Pu-O_{ax} SS paths. Only the Pu-O_{ax1}-Pu-O_{ax2} MS path is considered in our fits because other possible MS paths tend to cancel at a $k < 5Å^{-1}$. At k values larger than 5 $Å^{-1}$ MS amplitude contributions dampen out more quickly than SS amplitudes. This effect has been observed in the past for the uranyl moiety [40]. For the MS path, R_{MS} was set to $2R_{Oax}$, and the MS Debye-Waller (DW) factor was constrained to be twice the single-scattering (SS) DW factor ($\sigma^2_{MS} = 2\sigma^2_{SS}$) as was done in previous studies with uranyl [40].

The Pu-O_a path fits an unusually small plutonium-oxygen bond length of approximately 2.2 Å. Similar bond lengths have been reported in the literature [41] for uranyl and have been assigned as hydroxide complexation to the uranyl moiety, but to the best of our knowledge have not been reported for Pu-O bond lengths. Such bond length shortening could be the result of Pu(VI) bound to the mineral surface via a surface oxygen. At higher solution pH, more mineral

surface sites are deprotonated and available for binding in such a fashion. The Pu-O_b path fits to a bond length of approximately 2.37-2.40 Å, suggesting the presence of coordinated water around the plutonium atom. The increase in coordination number for Pu-O_b and decrease in coordination number for Pu-O_a as sample pH decreases implies hydroxide complexation (or Fe-O-Pu complexation) decreases and water coordination increases as the sample pH decreases, suggesting that our assignment above is correct.

The FT peak at approximately 3.0 Å fits well with a Pu-Fe bond length of approximately 3.33-3.36 Å. A Pu-Fe path was chosen for the model instead of a possible Pu-Mn path because of statistical reasons; it is simply more probable that plutonium will encounter a surface binding site which contains a distal iron atom as opposed to a distal manganese, assuming that site reactivity is similar for the two metal sites. Furthermore, it is not possible to differentiate a Pu-Fe path from a Pu-Mn path using the bulk XAS technique because of the similar scattering strengths of the iron and manganese atoms. Previous calculations and measurements collected on uranyl model compounds have shown that actinyl MS paths can also contribute to the FT peak at about 3.0 Å [39, 40]. This effect should be relatively small for our samples at higher pH since the majority of the plutonium is in the tetravalent form. Furthermore, the constraints on the plutonyl MS path imposed by the plutonyl SS path and geometric arguments take this effect into account for all sample fits. However, the large errors in the coordination number for the Pu-Fe path fit, in conjunction with the large DW factors, suggest the possibility of contributions from other paths. Most notably, a Pu-C scattering path could partially account for the FT peak at 3.0 Å. However, a fit without the Pu-Fe scattering path present results in an unreasonable number of carbons in that shell or a poor fit if the number of carbons is constrained. The MS from bi-dentate carbonate ligation is difficult to resolve as well because the EXAFS oscillations from the potential Pu-O_{dis}-C and Pu-C-O_{dis}-C paths are exactly π radians out of phase and of similar magnitude; that is, the EXAFS signal from these two MS paths destructively interfere with each other. Inspection of the speciation diagram shown in Figure 5 shows the possibility of carbonate coordination for the two higher pH samples. To take this possibility into account we conducted a modified F-test [42-44] to check for the significance of the Pu-Fe scattering path in the presence of a Pu-C scattering path in our fits. The results of the F-test are shown in Table 4 and represent our confidence that the Pu-Fe scattering path in our model is necessary to reproduce the spectral features of our data. Attempts were also made to fit Pu-Pu scattering paths, which would indicate Pu(IV) precipitation. Such attempts resulted in poor fits due to phase mismatch.

The fits presented in Table 4 have relatively large coordination numbers compared to the number of available coordination sites around the plutonium atom. This is particularly evident for sample MG-1.0, which fits 9.7 and 2.2 coordinated oxygens for scattering paths Pu-O_a and Pu-O_b, respectively. This is a result from coupling to a large DW factor. If σ is constrained to 0.08 Å approximately 6 and 2 oxygens are fit to the paths, respectively. Coordination numbers could also be inflated by roughly 10% due to errors in S_o^2, which has been artificially fixed at 1.0 for these fits. Furthermore the coordination numbers for the outer shells contain large associated error bars. Such large errors preclude any attempts to reconstruct the exact surface binding structure, but use of the F-test lends credence to our proposed Pu-Fe scattering path fit. This, in turn, allows us to confidently assign plutonium interaction with the surface as an inner-sphere complex.

4 Conclusions

We have shown direct spectroscopic evidence suggesting surface-mediated reduction of Pu(VI) to Pu(IV) on manganese-substituted goethite. The use of XAS allows for unambiguous, atom-specific determination of the oxidation state of plutonium in situ. However, the identity of the backscattering atom is currently unclear because iron and manganese have very similar EXAFS backscattering amplitudes. Bulk XAS measurements therefore cannot be used to clarify the identity of the distal metal bound to the plutonium atom. It is assumed that sorption is occurring on sites nearest a distal iron since manganese concentrations are low. However, past work has shown the preferential sorption of plutonium near manganese sites, even in minerals with low manganese concentrations [11, 12].

These results show the capacity of Mn-substituted goethite to reduce plutonium from Pu(VI) to the more insoluble Pu(IV) oxidation state. Knowledge of such reduction processes is essential in understanding the migration of plutonium through the geosphere and plays an important role in the proper modeling and risk-analysis of plutonium storage in underground geological repositories.

5 Acknowledgements

Portions of this work were supported by the Environmental Remediation Science Programs (ERSP) within the US Department of Energy's Office of Science, Climate and Environmental Sciences Division and the Office of Civilian Radioactive Waste Management Graduate Fellowship Program administered by Oak Ridge Institute for Science and Education under a contract between the U.S. Department of Energy (DOE) and Oak Ridge Associated Universities. Work at the Lawrence Berkeley National Laboratory (LBNL) was supported by the DOE under Contract No. DE-AC02-05CH11231. Work at the Savannah River National Laboratory (SRNL) was conducted under DOE contract DE-AC09-96SR18500.

XAS measurements were carried out at the Stanford Synchrotron Radiation Lightsource, a national user facility operated by Stanford University on behalf of the U.S. Department of Energy, Office of Basic Energy Sciences. The SSRL Structural Molecular Biology Program is supported by the Department of Energy, Office of Biological and Environmental Research, and by the National Institutes of Health, National Center for Research Resources, Biomedical Technology Program.

Mössbauer spectroscopy measurements were conducted at the Environmental Molecular Sciences Laboratory (EMSL), a national scientific user facility sponsored by DOE's Office of Biological and Environmental Research program. EMSL is located at the PNNL in Richland, WA, USA.

Disclaimer

authors expressed herein do not necessarily state or reflect those of the United States Government or any agency thereof or The Regents of the University of California.

6 References

1. Cleveland, J. M. *The Chemistry of Plutonium*; American Nuclear Society, 1979.
2. Choppin, G. R.: Radiochim. Acta, **91**, 645-649 (2003).
3. Choppin, G. R.; Rao, L. F.: Radiochim. Acta, **37**, 143-146 (1984).
4. Kaplan, D. I.; Powell, B. A.; Demirkanli, D. I., et al.: Environ. Sci. Technol., **38**, 5053-5058 (2004).
5. Shaughnessy, D. A.; Nitsche, H.; Booth, C. H., et al.: Environ. Sci. Technol., **37**, 3367-3374 (2003).
6. Powell, B. A.; Fjeld, R. A.; Kaplan, D. I., et al.: Environ. Sci. Technol., **38**, 6016-6024 (2004).
7. Powell, B. A.; Duff, M. C.; Kaplan, D. I., et al.: Environ. Sci. Technol., **40**, 3508-3514 (2006).
8. Wilson, R. E., Thesis, Reactions of Plutonium(VI) with the Iron Oxide Goethite, University of California, Berkeley, Berkeley, 2005.
9. Powell, B. A.; Fjeld, R. A.; Kaplan, D. I., et al.: Environ. Sci. Technol., **39**, 2107-2114 (2005).
10. Keeney-Kennicutt, W. L.; Morse, J. W.: Geochim. Cosmochim. Acta, **49**, 2577-2588 (1985).
11. Duff, M. C.; Hunter, D. B.; Triay, I. R., et al.: Environ. Sci. Technol., **33**, 2163-2169 (1999).
12. Duff, M. C.; Newville, M.; Hunter, D. B., et al.: J. Synchrotron Radiat., **6**, 350-352 (1999).
13. Schwertmann, U.; Cornell, R. M. *Iron Oxides in the Laboratory: Preparation and Characterization*; VCH Publishers, 1991.
14. Cornell, R. M.; Giovanoli, R.: Clay Clay Min., **35**, 11-20 (1987).
15. Stiers, W.; Schwertmann, U.: Geochim. Cosmochim. Acta, **49**, 1909-1911 (1985).
16. Cristiano, E.; Hu, Y.-J.; Siegfried, M. M., et al.: "Critical Measurements of the Point-of-Zero-Charge Values for Synthetic Goethite and Pyrolusite" submitted to J. Environ. Qual.
17. Mustafa, S.; Dilara, B.; Nargis, K., et al.: Colloid Surf. A-Physicochem. Eng. Asp., **205**, 273-282 (2002).
18. Stumm, W. *Chemistry of the Solid-Water Interface*, 2nd ed.; J.Wiley & Sons, Inc., 1992.
19. Noh, J. S.; Schwarz, J. A.: J. Colloid Interf. Sci., **130**, 157-164 (1989).
20. Ping, J. Y.; Rancourt, D. G.; Stadnik, Z. M.: Hyperfine Interact., **69**, 493-496 (1991).

21. Guillaumont, R.; Fanghänel, T.; Neck, V., et al. *Update on the Chemical Thermodynamics of Uranium, Neptunium, Plutonium, Americium and Technetium*; Elsevier, 2003.

22. Matsumoto, M.; Nishimura, T.: ACM Trans. Model. Comput. Simul., **8**, 3-30 (1998).

23. Parkhurst, D. L.; Appelo, C. A. J., *User's guide to PHREEQC (Version 2) -- a computer program for speciation, batch-reaction, one-dimensional transport, and inverse geochemical calculations*, U.S. Geological Survey Water-Resources Investigations Report 99-4259 (1999).

24. Cohen, D.: J. Inorg. Nucl. Chem., **18**, 211-218 (1961).

25. Hu, Y.-J.; Booth, C. H.: J. Phys. Conf. Ser., **190** (2009).

26. Booth, C. H. (2006) Available at http://lise.lbl.gov/RSXAP/

27. Li, G. G.; Bridges, F.; Booth, C. H.: Phys. Rev. B, **52**, 6332-6348 (1995).

28. McMaster, W. H.; Kerr Del Grande, N.; Mallett, J. H., et al., *Compilation of X-ray Cross Sections*, UCRL-50174 Section II Revision I (1969).

29. Conradson, S. D.; Abney, K. D.; Begg, B. D., et al.: Inorg. Chem., **43**, 116-131 (2003).

30. Conradson, S. D.: Appl. Spectrosc., **52**, 252A-279A (1998).

31. Zabinsky, S. I.; Rehr, J. J.; Ankudinov, A., et al.: Phys. Rev. B, **52**, 2995-3009 (1995).

32. Stern, E. A.: Phys. Rev. B, **48**, 9825-9827 (1993).

33. Booth, C. H.; Hu, Y.-J.: J. Phys. Conf. Ser., **190** (2009).

34. Sileo, E. E.; Alvarez, M.; Rueda, E. H.: Int. J. Inorg. Mater., **3**, 271-279 (2001).

35. Alvarez, M.; Rueda, E. H.; Sileo, E. E.: Geochim. Cosmochim. Acta, **71**, 1009-1020 (2007).

36. Cornell, R. M.; Schwertmann, U. *The Iron Oxides*; John Wiley & Sons Ltd., 1997.

37. Ekberg, C.; Ödegaard-Jensen, A.; Meinrath, G., *LJUNGSKILE 1.0: A computer Program for Investigation of Uncertainties in Chemical Speciation*, SKI Report 2003:03 (2002).

38. Ödegaard-Jensen, A.; Ekberg, C.; Meinrath, G.: Talanta, **63**, 907-916 (2004).

39. Allen, P. G.; Bucher, J. J.; Clark, D. L., et al.: Inorg. Chem., **34**, 4797-4807 (1995).

40. Hudson, E. A.; Allen, P. G.; Terminello, L. J., et al.: Phys. Rev. B, **54**, 156 (1996).

41. Clark, D. L.; Conradson, S. D.; Donohoe, R. J., et al.: Inorg. Chem., **38**, 1456-1466 (1999).

42. Bacchi, A.; Lamzin, V. S.; Wilson, K. S.: Acta Crystallographica, Section D-Biological Crystallography, **52**, 641-646 (1996).

442 43. Downward, L.; Booth, C. H.; Lukens, W. W., et al. 2006; AIP Conference Proceedings; 129.

443 44. Hamilton, W. C.: Acta Crystallogr., **18**, 502 (1965).

444

445

Captions

Table 1. Characterization data for the two Mn-substituted goethite minerals used in this study. Error bars are presented at the 1σ confidence level.

Table 2. Thermodynamic data for the hydrolysis and formation of carbonate species in aqueous solution for Pu(VI) taken from Guillaumont et al. [21]. Error bars represent a 95% confidence interval.

Table 3. Least-squares fits of Pu L_{III}-edge XANES data to Pu(IV), Pu(V), and Pu(VI) standard spectra. Fits consistently returned zero fit contribution from the Pu(VI) standard spectra. Error bars are presented at the 1σ confidence level.

Table 4. Fit parameter results from Pu L_{III}-edge EXAFS fits. Symmetric and asymmetric error bars are presented at the 1σ confidence level.

Figure 1. Powder XRD spectra of goethite and Mn-substituted goethite.

Figure 2. Scanning electron micrograph images of the 63-212 μm size fraction of goethite (left) and MG-1.0 (right). Upon inspection of the micrographs (in the 1μm range) the following morphologies are seen: round rod-like structures for pure goethite and an increase in the length-to-width ratio in crystal growth for Mn-substituted goethite as compared to pure goethite.

Figure 3. Room temperature Mössbauer spectra (a) and the modeled hyperfine field distribution (b) for Mn-substituted goethite samples.

Figure 4. Manganese K-edge XANES spectra for Mn-substituted goethite and reference compounds. Reference scan for $Mn^{II}SO_4$, $LaMn^{III}O_3$, and $CaMn^{IV}O_3$ taken from Alvarez et.al. [35]. A dashed line is drawn at the peak position of the $LaMn^{III}O_3$ reference compound and shows that manganese in the Mn-substituted goethite is incorporated into the mineral structure as Mn(III).

Figure 5. Pu(VI) speciation diagram calculated using the in-house code SPECIATE. Middle bands represent the average species. Upper and lower bands represent error propagated through the thermodynamic constants into the speciation diagram at the 1σ level. Thermodynamic data used to calculate this diagram is shown in Table 2 and taken from Guillaumont et al. [21]. The plutonium species $(PuO_2)_2(OH)_2$ never exceeded 1% of the total solution species and was not plotted for sake of clarity.

Figure 6. Representative plutonium L_{III}-edge XANES spectra for Pu(VI) sorbed on Mn-substituted goethite. The energy was calibrated by setting the first inflection point of the Pu L_{III} edge of a PuO_2 reference sample to be 18062.3 eV [29]. Approximately 35% of the plutonium was Pu(IV) and 65% was Pu(V). Error in the fit at 1σ confidence is 3%.

Figure 7. EXAFS spectra fits in k^3-weighted $\chi(k)$ vs. k, the photoelectron wave vector (left column) and the corresponding Fourier transform magnitude vs. $r + \Delta$, the pseudo-radial distribution function (right column). Solid black lines are Fourier-filtered data and the dashed grey lines are the associated fits. The position of the Pu-Fe scattering path is at roughly 3.0 $r + \Delta$.

493 **Tables**

494

Mn-sub goethite	% Mn substitution[a]	BET surface area ($m^2 \cdot g^{-1}$)	PZC
MG-1.0	1.0 ± 0.2	19.7	6.46 ± 0.09
MG-0.5	0.5 ± 0.1	13.9	6.78 ± 0.05
pure goethite	0.051 ± 0.007	32.8	7.46 ± 0.02

a. %Mn substitution expressed as (Mn)/(Mn+Fe)*100

495 **Table 1.**

496

497

498

499

500

501

502

503

504

505

Reaction	$\log_{10}\beta^o$	Reference
Hydrolysis Complexes		
$PuO_2^{2+} + H_2O \leftrightarrow PuO_2OH^+ + H^+$	-5.5 ± 0.5	[21]
$PuO_2^{2+} + 2\ H_2O \leftrightarrow PuO_2(OH)_2 + 2\ H^+$	-13.2 ± 1.5	[21]
$2\ PuO_2^{2+} + 2\ H_2O \leftrightarrow (PuO_2)_2(OH)_2^{2+} + 2\ H^+$	-7.5 ± 1.0	[21]
Carbonate Complexes		
$PuO_2^{2+} + CO_3^{2-} \leftrightarrow PuO_2CO_3$	9.5 ± 0.5	[21]
$PuO_2^{2+} + 2\ CO_3^{2-} \leftrightarrow PuO_2(CO_3)_2^{2-}$	14.7 ± 0.5	[21]
$PuO_2^{2+} + 3\ CO_3^{2-} \leftrightarrow PuO_2(CO_3)_3^{4-}$	18.0 ± 0.5	[21]

506 **Table 2.**

507

508

509

510

511

512

513

514

515

516

Sample	PZC	Solution pH	% Pu Sorbed	% Pu(IV)	% Pu(V)
MG-1.0	6.46 ± 0.09	8.05 ± 0.05	35.6 ± 0.3	71 ± 8	29 ± 9
MG-0.5	6.78 ± 0.05	7.63 ± 0.05	46.8 ± 0.3	74 ± 6	26 ± 7
MG-0.5	6.78 ± 0.05	6.05 ± 0.05	43.5 ± 0.3	35 ± 3	65 ± 3

517 **Table 3.**

518

Sample	Solution pH	Scattering Path	R(Å)	N	σ(Å)	ΔE_o[a]
MG-1.0	8.05 ± 0.05	Pu-O_{ax1}	1.89 ± 0.02	0.58[b]	0.03[c]	$-5.2^{+3.2}_{-2.4}$
		Pu-O_{ax1}-Pu-O_{ax2}	3.78[d]	0.58[d]	0.06[d]	
		Pu-O_a	2.23 ± 0.02	$9.7^{+1.0}_{-1.2}$	0.11 ± 0.01	
		Pu-O_b	$2.4^{+0.3}_{-1.4}$	$2.2^{+1.0}_{-1.4}$	0.11[e]	
		Pu-Fe	$3.36^{+0.02}_{-0.03}$	$2.17^{+2.5}_{-0.7}$	0.08 ± 0.03	
R(%) = 11.22						
F-Test for Pu-Fe Path Significance = 94.31%						
MG-0.5	7.63 ± 0.05	Pu-O_{ax1}	$1.91^{+0.04}_{-0.02}$	0.52[b]	0.03[c]	-5.1 ± 1.3
		Pu-O_{ax1}-Pu-O_{ax2}	3.83[d]	0.52[d]	0.06[d]	
		Pu-O_a	2.21 ± 0.02	$5.6^{+0.9}_{-0.8}$	$0.07^{+0.01}_{-0.03}$	
		Pu-O_b	2.37 ± 0.02	4.1 ± 0.3	0.07[e]	
		Pu-Fe	3.35 ± 0.02	$5.4^{+6.1}_{-3.0}$	0.15 ± 0.03	
R(%) = 10.07						
F-Test for Pu-Fe Path Significance = 91.67%						
MG-0.5	6.05 ± 0.05	Pu-O_{ax1}	1.85 ± 0.02	1.3[b]	0.07 ± 0.02	-2.3 ± 2.1
		Pu-O_{ax1}-Pu-O_{ax2}	3.71[d]	1.3[d]	0.14[d]	
		Pu-O_a	2.19 ± 0.02	$4.7^{+1.4}_{-0.7}$	0.08 ± 0.01	
		Pu-O_b	2.40 ± 0.02	$6.5^{+1.6}_{-1.2}$	0.08[e]	
		Pu-Fe	$3.33^{+0.03}_{-0.02}$	$5.4^{+6.1}_{-3.0}$	$0.14^{+0.04}_{-0.14}$	
R(%) = 13.08						
F-Test for Pu-Fe Path Significance = 69.26%						

[a]ΔE_o was set to be the same for all paths.
[b]SS plutonyl oxygen coordination number constrained to data acquired from XANES
[c]SS plutonyl oxygen Debye-Waller factor constrained to 0.03Å.
[d]MS plutonyl oxygen bond lengths, coordination number and Debye-Waller factors constrained to single scattering path [40].
[e]Pu-O_b Debye-Waller factor constrained to Pu-O_a.

519
520 **Table 4.**
521

Figures and Captions

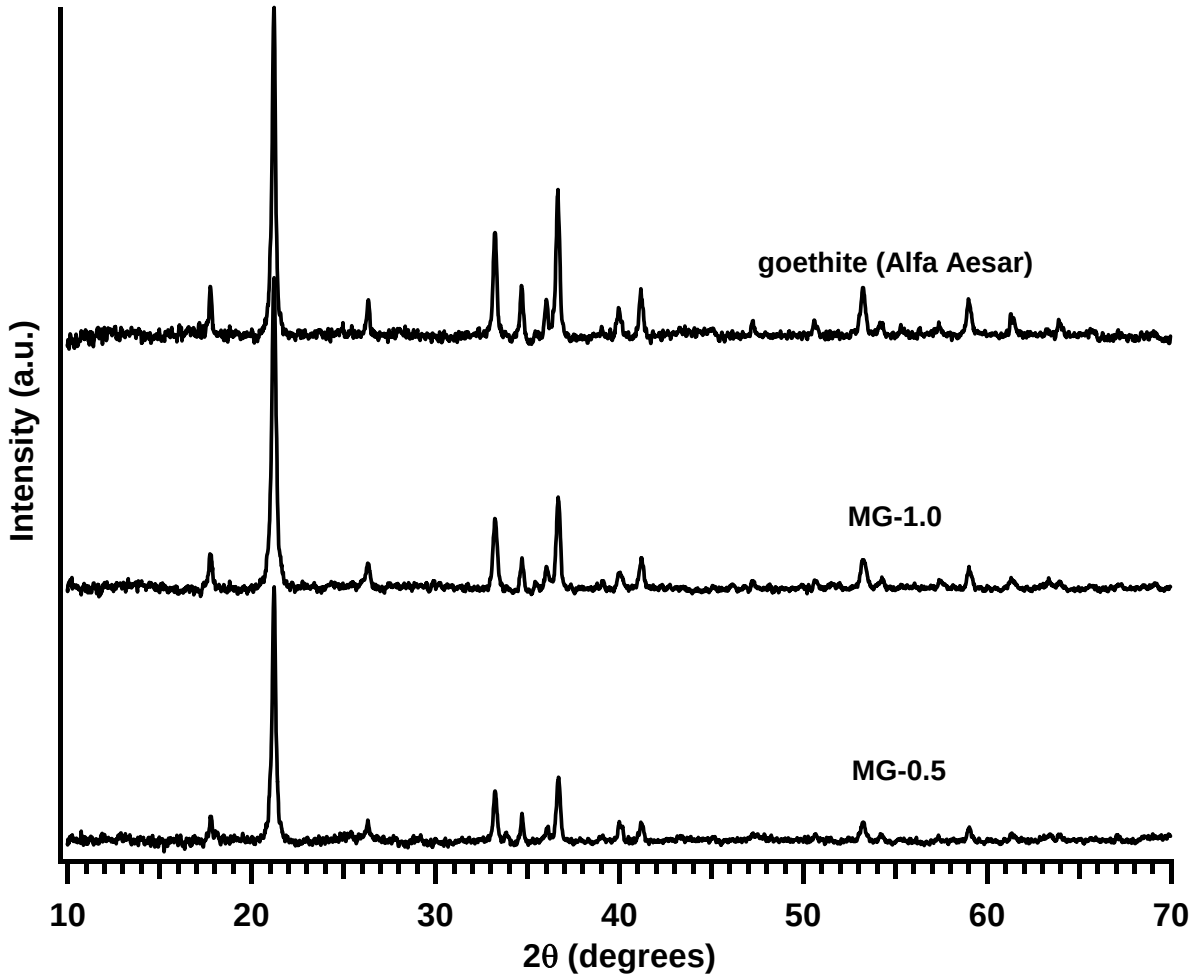

Figure 1.

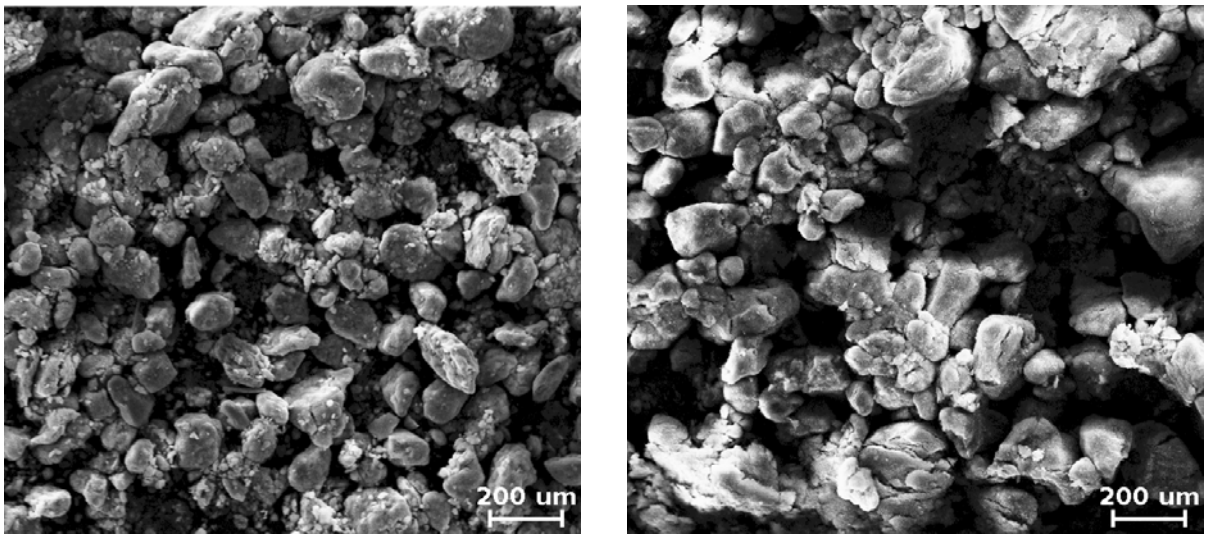

Figure 2.

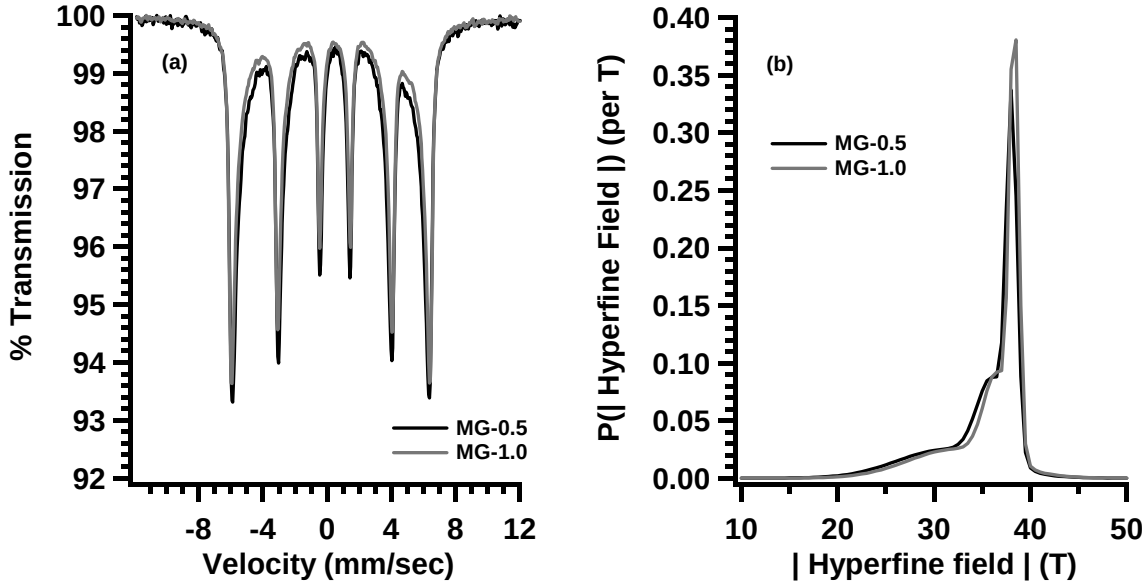

Figure 3.

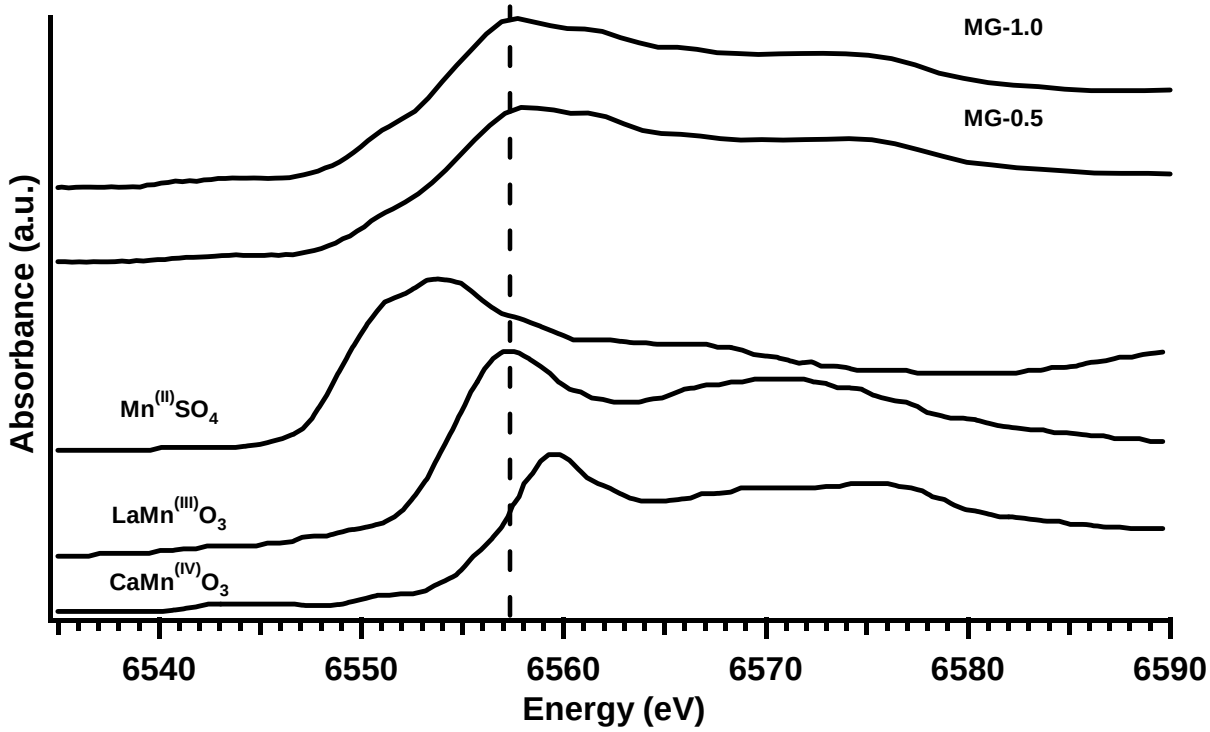

Figure 4.

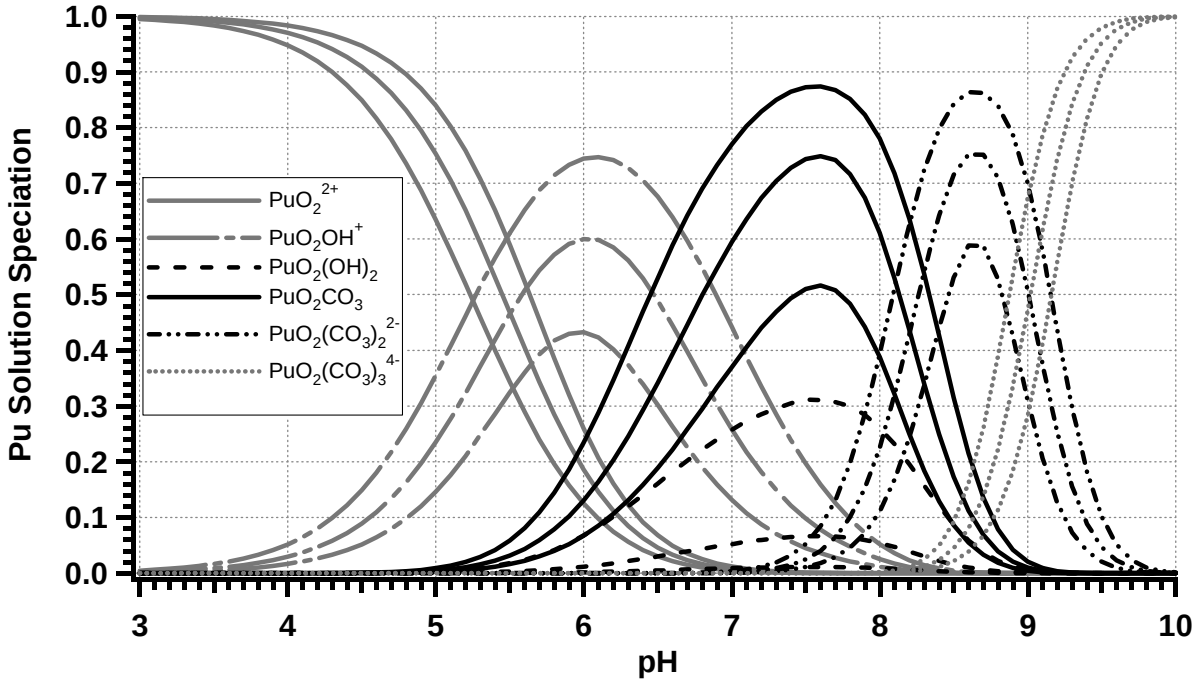

Figure 5.

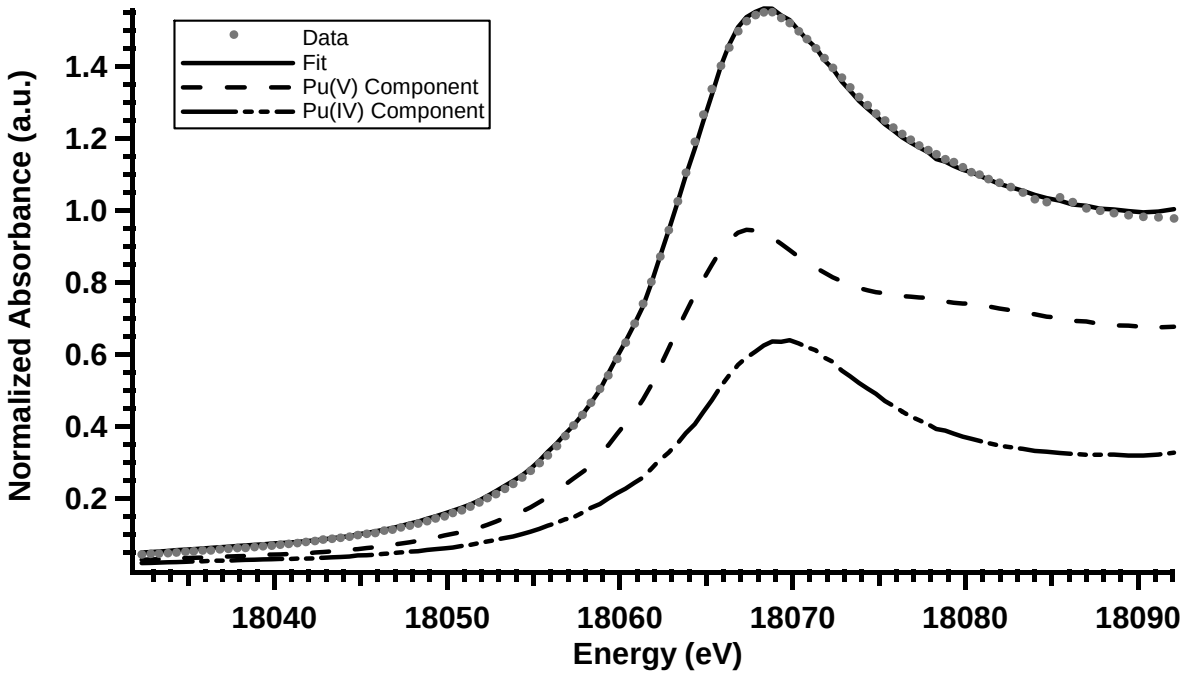

Figure 6.

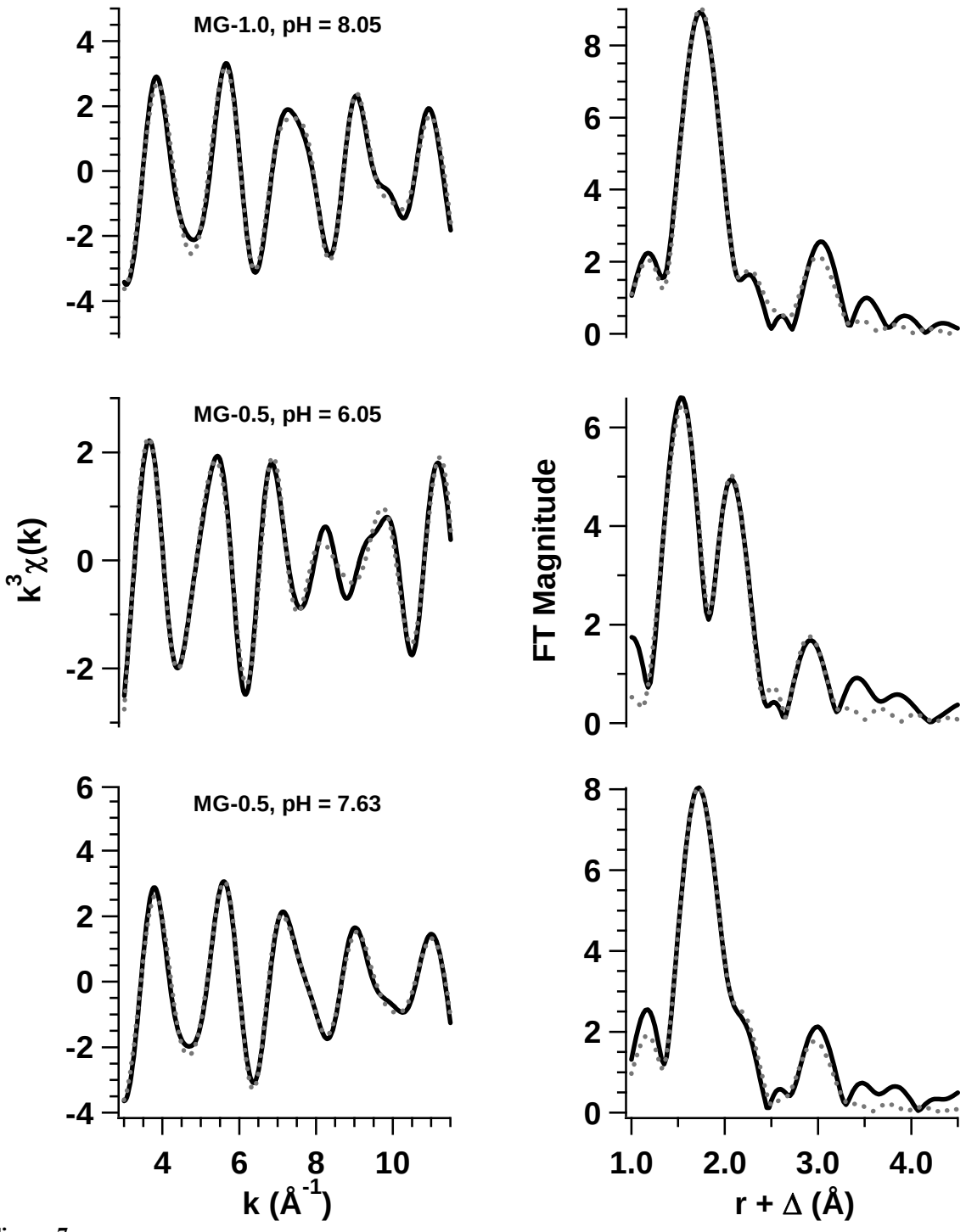

Figure 7.